Applied Physics A (2023) 129:57
https://doi.org/10.1007/s00339-022-06333-y

Applied Physics A
Materials Science & Processing

Carbon-wrapped amorphous Ni–Co binary oxide nanosheet for high-performance pseudocapacitors

Jialin Guo[1] · Wenjing Li[2] · Peng Zheng[3]

Received: 13 November 2022 / Accepted: 12 December 2022 / Published online: 23 December 2022

Abstract

The development of high-energy density supercapacitor demands that the electrode has the characteristic of good conductivity for electron and open framework structure and ion transfer. $NiCo_2O_4$ already exhibits superior electric conductivity among the multi-metal oxides. Here, carbon-wrapped amorphous Ni–Co oxide nanosheet is prepared by a hydrothermal method, followed by an annealing process in Ar atmosphere. The conductivity is further improved by carbon coating and it also has a more open structure, which is verified by extended X-ray absorption fine structure analysis. Owing to the advantage of its structure, the carbon-wrapped amorphous Ni–Co oxide shows large capacitance of 1775 F g^{-1} at 1 A g^{-1} in three-electrode aqueous system, high energy density of 73.5 Wh kg^{-1} and power density of 806.7 W kg^{-1} in asymmetric supercapacitors. The open framework feature of the amorphous would promote the wide exploration of amorphous Ni–Co oxide material as the electrode for energy storage devices.

Keywords Amorphous Ni–Co oxide · Supercapacitor · Cathode · Nanosheet · Open framework structure

1 Introduction

As the cathode of supercapacitor, transition metal oxides(such as MnO_2, NiO and Co_3O_4) could provide additional pseudo-capacitance for higher energy density compared with the electrostatic double layer capacitors. The development of energy conversion device of hybrid electric vehicles (HEVs) and electric vehicles (EVs) needs high power and energy density simultaneously in one system [1–3]. To meet the requirement, as the merit of high power density of supercapacitor, it is needed to further improve the energy density [4, 5]. As the diverse metal centers with rich redox reaction offer more electrochemical active sites for the multi-transition metal oxides, they have been given intensive attention recently. Among the synthesized binary metal oxides (such as $ZnCo_2O_4$ [6, 7], $NiMoO_4$ [8], $MnMoO_4$ [9], $FeMnO_3$ [10] and $CuCo_2O_4$ [11]), nickel cobaltite oxide ($NiCo_2O_4$) is the most widely investigated pseudo-capacitive materials, due to the additional merit of high electric conductivity, which is at least two orders magnitude higher than that of either nickel oxides or cobalt oxides. Various morphologies of $NiCo_2O_4$ have been reported, including nanosheet [12, 13], nanowire [14, 15], sphere [16, 17], nanotube [18] and nanocube [19]. For higher rate performance, coupling with various carbons (such as graphene [20], tube [21], fiber and coating layer [22]) is a common strategy, due to the enhanced electric conductivity via carbon. Besides the single-phase $NiCo_2O_4$, some non-stoichiometric compositions (such as $Ni_{0.3}Co_{2.7}O_4$ [23], Ni–Co oxide nanosheets [24] and NiCoAl layered hydroxide) also exhibit high capacitance. Diversified composition and structure of Ni–Co oxide may offer more opportunity for good performance.

Apart from the above-mentioned crystal structure, amorphous materials also have been widely applied, especially in catalysis [25, 26] and electrochemistry [27–29]. For electrochemistry, the disordered (short-range ordered) structure has a lower entropic energy incorporated of out ions and a

Jialin Guo and Wenjing Li have contributed equally.

✉ Peng Zheng
zhengpeng@sust.edu.cn

[1] Shaanxi Key Laboratory of Comprehensive Utilization of Tailings Resources, College of Chemical Engineering and Modern Materials, Shang Luo University, Shang Luo 726000, Shaanxi, People's Republic of China

[2] Xi'an International Medical Center Hospital, Xian 710021, Shaanxi, People's Republic of China

[3] School of Materials Science and Engineering, Shaanxi University of Science and Technology, Xian 710021, Shaanxi, People's Republic of China

more open framework for out-ion transport; such characteristics are beneficial to improve the electrochemical performance [30, 31]. For instance, it is widely confirmed that the amorphous $FePO_4$ has better electrochemical activity than the crystalline one [31–33]; Cao et al. [34]. demonstrated that amorphous vanadium oxide has higher capacity than its crystalline counterpart for sodium-ion battery; Lu et al. [35] reported that amorphous NiO has higher capacitance than the crystalline one; Li et al. [30] also showed that amorphous nickel hydroxide has better capacitance than the crystalline one. Motivated by the above amorphous cases and the promising new structure of Ni–Co oxide, evaluating amorphous Ni–Co oxide electrode as a supercapacitor is very attractive [36, 37].

In this report, carbon-wrapped amorphous Ni–Co binary oxide sphere comprising nanosheets is prepared via a hydrothermal method, followed by annealing under an Ar atmosphere. It shows a high capacitance of 1775 F g^{-1} at 1 A g^{-1}. However, when the same hydrothermal precursor is annealed under air atmosphere, the product is crystal $NiCoO_2$ nanoparticles, which only shows a capacitance of 1140 F g^{-1} at 1 A g^{-1}. The capacitance of the amorphous form is 1.56 time higher than the crystal $NiCoO_2$, which could be attributed to the open frame and high conduction of the amorphous structure. The amorphous form displays large energy (73.5 Wh kg^{-1}) and power (806.7 W kg^{-1}) density in asymmetric supercapacitors.

2 Experimental section

2.1 Synthesis

The precursor was obtained by a facile hydrothermal treatment. The starting materials of 2.93 mM $CoCl_2{\cdot}6H_2O$, 1.47 mM $Ni(NO_3)_2{\cdot}6H_2O$, 80 ml EtOH and 2 g furfural were placed in a 100 ml Teflon-lined stainless steel autoclave. After stirring for 1 h, the mixture was heated to 140 °C for 10 h. The autoclave was then cooled to room temperature naturally. The precipitate was collected by centrifugation, washed with deionized water and ethanol, and dried at 60 °C for 10 h. To prepare carbon-wrapped amorphous Ni–Co oxide, the hydrothermal precursor was annealed under Ar environment at 300 °C for 2 h with a heating rate of 3 °C min^{-1}.To synthesize $NiCoO_2$ nanoparticles, the hydrothermal precursor was annealed under the same condition as carbon-wrapped amorphous Ni–Co oxide except using an air environment.

2.2 Characterization

Scanning electron microscope (SEM) S4800 and high-resolution transmission electron microscope (HRTEM) FEI Tecnai F20 were used to observe the morphologies. The structure was detected by the X-ray diffraction (XRD) patterns using Bruker D8 Advanced X-ray, X-ray photoelectron spectroscopy (XPS) using Kratos Axis Suppa spectrograph and N_2 adsorption – desorption isotherms using ASAP2000. The Co/Ni L-edge and O K-edge X-ray absorption near edge structure (XANES) measurements were carried out at the spherical grating monochromator BL20a1 beamline at the Taiwan Light Source. XANES and X-ray absorption fine structure (EXAFS) spectra were collected at Beijing Synchrotron Radiation Facility for Co and Ni K-edge. Athena software package was employed with all the spectra.

2.3 Electrochemistry

The working electrode was prepared by mixing 80 wt % of the prepared product, 10 wt % of acetylene black and 10 wt % of polytetrafluoroethylene (PTFE) in the presence of alcohol. After the components were thoroughly mixed, the slurry was dropped onto a nickel foam (about 4 mg /cm^2). Finally, the electrodes were dried for 4 h at 110 °C in air and pressed at 10 MPa.

For the three-electrode system test, the working electrode, counter electrode (platinum wire) and reference electrode (saturated calomel electrode) were put in the in 2 M KOH aqueous electrolyte. Cyclic voltammetry (CV) and galvanostatic charge/discharge (GCD) tests were performed in the range of 0–0.4 V (vs SCE). The average specific capacitance was calculated according to the galvanostatic discharge curve using the equation of $C = I \times \Delta t/(\Delta V \times m)$. For the asymmetric supercapacitor, a sandwich-type construction (electrode/separator/electrode) of coin cell 2032 was used.

In the measured two-electrode system, working electrode, prepared activated carbon, Whatman filter paper and 1 M KOH solution were the positive electrode, negative electrode, separator and electrolyte, respectively. To balance stored charge between positive electrode and negative electrode, the loading mass ratio of carbon-wrapped amorphous Ni–Co oxide and activated carbon was employed. Equations $C = 2I \times \Delta t/(\Delta V \times m)$, $E = (1/8)\, C \times \Delta V^2$, $P = E/\Delta t$ were used to calculate the specific capacitance, energy density and power density of symmetrical supercapacitor systems, respectively. The above-mentioned Δt, I, ΔV, m, P and E are the discharging time, applied current, potential window, mass, power density and energy density, respectively. All the electrochemical performance was performed on the CHI 660E electrochemical station.

3 Results and discussion

The precursor is a sphere composed of nanosheet (Fig. S1), obtained through hydrothermal treatment at 140 °C for 10 h using $CoCl_2{\cdot}6H_2O$, $Ni(NO_3)_2{\cdot}6H_2O$ and furfural as starting materials. XRD technique is a powerful tool to determine the crystallinity and phase of all solid samples. When the precursor is annealed under Ar atmosphere at 300 °C for 2 h, the resulting sample is amorphous (denoted as C@ amorphous Ni–Co oxide), as indicated by the non-peak curve of Fig. 1a. As shown in Fig. 1b, it is sphere for amorphous Ni–Co oxide, which is also composed by nanosheet with the thickness of dozens of nanometer (the inset of Fig. 1b). The amorphous feature could also be revealed by the HRTEM image through the disorder stripes (Fig. 1c), and a thin carbon layer is observed at the edge of the nanosheet. The evidence of carbon coating layer could be further verified by element mapping (Fig. S2), in which C has less content but the distribution as the same shape with Ni, Co and O, thus confirming carbon is coated on the surface of the nanosheet, the coating layer is benefit to enhance the conductivity. Figure 1d displays the nitrogen adsorption–desorption isotherms of C@ amorphous Ni–Co oxide. An obvious hysteresis loop suggests a porous structure and the Brunauer–Emmett–Teller (BET) surface area is 94.7 $m^2\ g^{-1}$, which favor electrolyte diffusion. However, when the precursor is annealed under air atmosphere under the same condition as C@ amorphous Ni–Co oxide, the resulting sample is indexed to cubic $NiCoO_2$ (PDF#10–0188) (Fig. 1e), and the morphology is changed into nanoparticles (Fig. 1f).

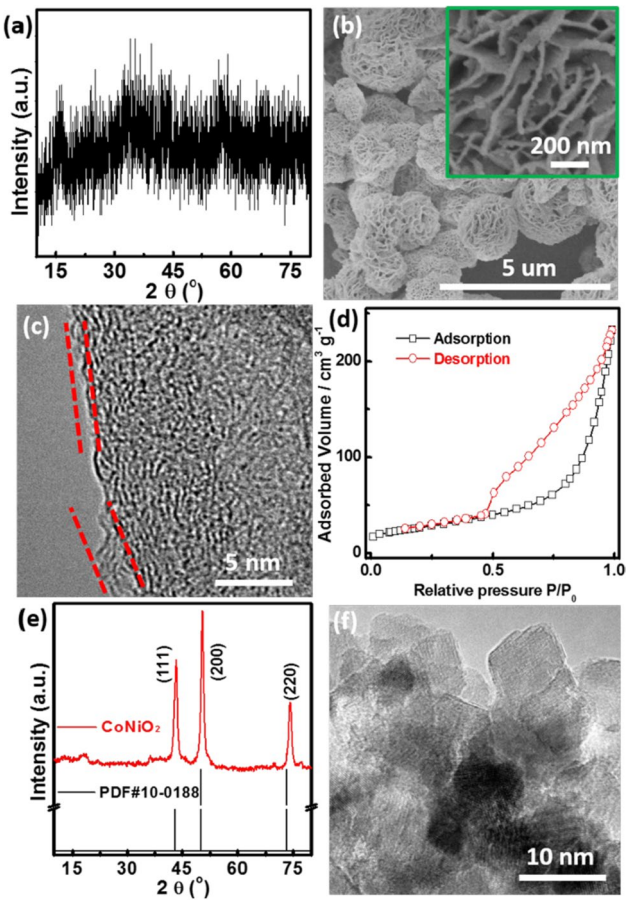

Fig. 1 **a** XRD pattern; **b** SEM image, the inset is the enlarged image; **c** HRTEM image; and **d** nitrogen adsorption–desorption isotherms of C@ amorphous Ni–Co oxide. **e** XRD pattern and **f** HRTEM image of $NiCoO_2$

The XPS technique can provide the chemical composition and oxidation state of the surface structure. As shown by Fig. 2a, by applying a Gaussian fitting, four peaks are deconvoluted for Co2p. The fitting peaks at 780.0 and 796.2 eV are assigned to the spin–orbit characteristics of Co^{2+}. The other fitting peaks are attributed to shake-up satellites (denoted as "Sat.") [38]. For the Ni 2p XPS (Fig. 2b), the main $2p_{3/2}$ and $2p_{1/2}$ peaks are attributed to Ni^{2+} at the binding energy of 856.3 and 874.1 eV. For the O1s spectra (Fig. 2c), it was deconvoluted into three types of oxygen species labeled as O^1, O^2 and O^3. The peak at 529.7 eV of O^1 is typical of metal – oxygen bonds. O^2 sited at 531.1 eV corresponds to the defect state occurring due to the low coordination number of oxygen. The weak peak of O^3 (≈533.32 eV) is attributed to the multiplicity of physic-/chemisorbed water at/within the interface of the amorphous [39]. XAS is a power technique to probe the electronic states of complex materials and structure information of bulk materials, which is based on the movement of excited electrons from core level to local and partially empty states. Figure 2d displays the O K-edge XAS spectrum of the C@ amorphous Ni–Co oxide. The two pre-edge peaks below 534 eV are attributed to the hybridized state of the oxygen 2p and transition metal 3d orbital, and the broad peak above 534 eV is assigned to the hybridization between oxygen 2p and transition metal 4 s and 4p orbitals. The peaks blurred in the spectrum of C@ amorphous Ni–Co oxide are similar to the characteristic of the CoO due to the distorted crystal symmetry. As shown by Fig. 2e, the Co $L_{2,3}$-edge XAS spectral profile of C@ amorphous Ni–Co oxide is nearly the same as that of CoO (Co^{2+}) and is slightly different from that of $NiCo_2O_4$ crystal due to the distorted chemical environment of Co by additional Ni. The Ni $L_{2,3}$-edge XAS spectrum (Fig. 2f) of the C@ amorphous Ni–Co oxide also shows nearly identical features to those of $NiCo_2O_4$ crystal, suggesting that Ni in the amorphous sample is in the form of $NiCo_2O_4$ in a lower oxidation state (Ni^{2+}). These information from bulk are in consistent with that form surface XPS analysis. The carbon content is 18 wt%, estimated by the TG curve (Fig. 3), using the precursor as the start material.

Co and Ni K-edge X-ray absorption near edge structure (XANES) plots and the k^3-weighted Fourier transform

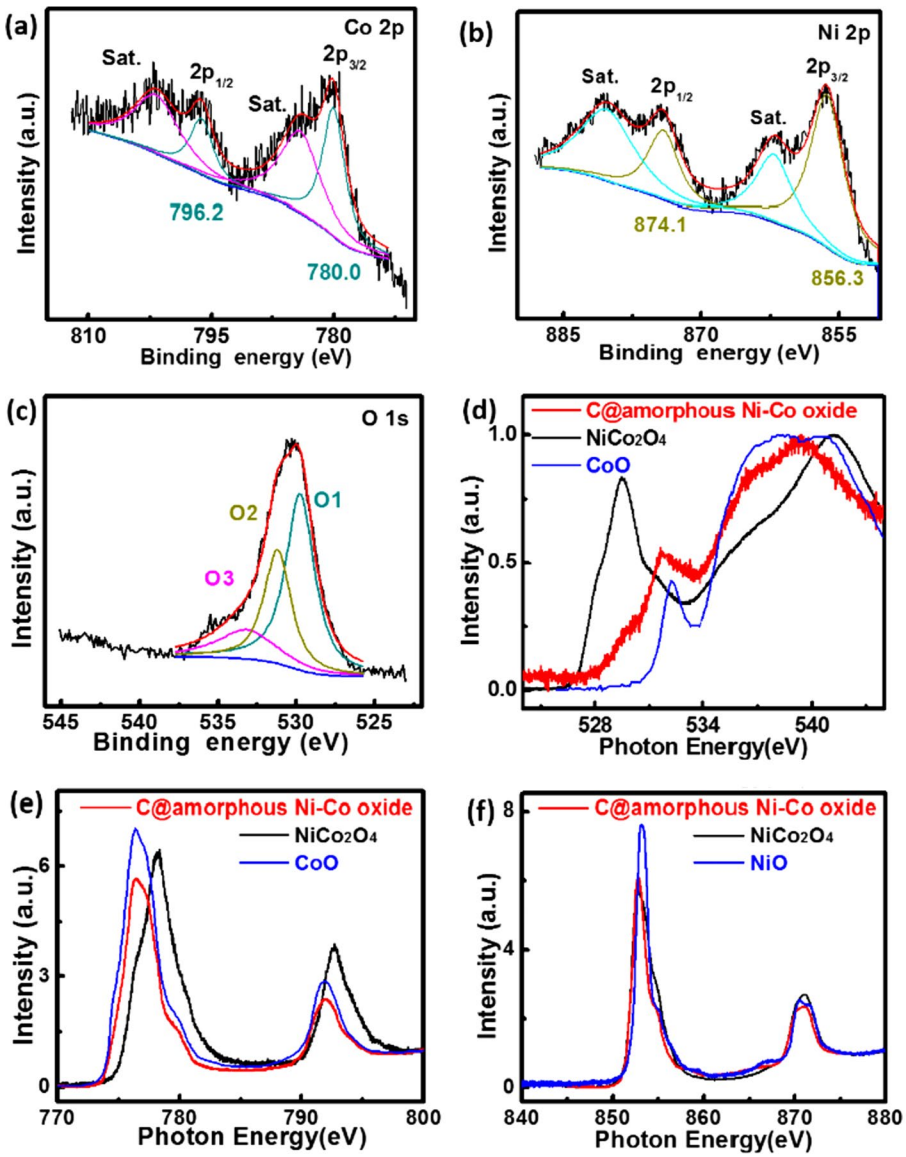

Fig. 2 **a** Co2p, **b** Ni2p and **c** O1s high-resolution XPS spectra of C@ amorphous Ni–Co oxide. **d** O K-edge, **e** Co L-edge and **f** Ni L-edge of C@ amorphous Ni–Co oxide and its metal oxides

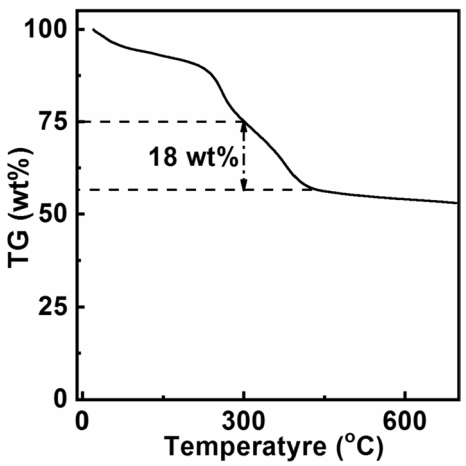

Fig. 3 TG curve of the precursor

of extended X-ray absorption fine structure (EXAFS) are shown in Fig. 4. The absorption edge itself is involved in the 1s to 4p dipole transition, while the pre-edge peaks in the XANES spectra are assigned to the 1s to 3d electronic transition. The decreased intensity in the pre-edge peak indicates an increased distance between cobalt and oxygen atom. Information on the coordination shell distance between atomic neighbors could be resolved from EXAFS. The Fourier transforms show the radial structure functions for the central absorbing 3d transition metal atoms and highlights the variation in the local structures between the amorphous and crystalline Ni–Co oxide. The amplitude of the peaks for the C@amorphous Ni–Co oxide is lower than that of $NiCo_2O_4$, which suggests that the amorphous material has a high structural disorder degree and diminished extending coordination. Crystalline $NiCo_2O_4$ shows well-defined peaks

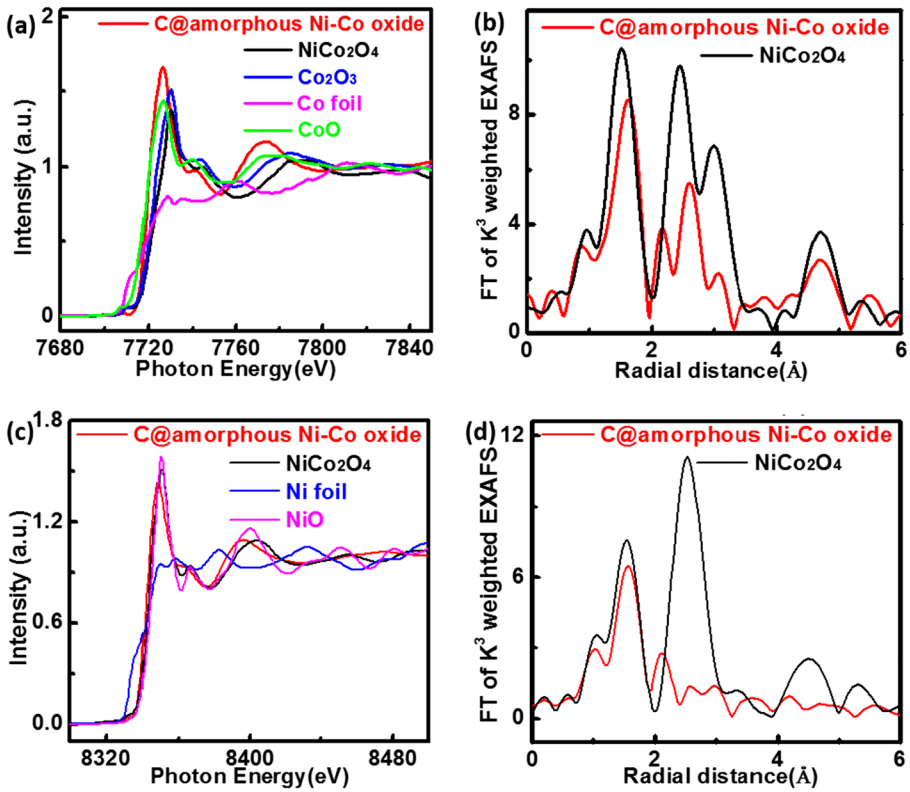

Fig. 4 **a** Co K-edge and **c** Ni K-edge of C@amorphous Ni–Co oxide and its metal oxides; **b** k^3-weighted Fourier transform of the Co k-edge EXAFS and **b** k^3-weighted Fourier transform of the Ni K-edge EXAFS of the C@amorphous Ni–Co oxide and $NiCo_2O_4$

at 1.50 and 2.50 Å, which are derived from the Co–O single scatter contribution (1st coordination sphere) and Co–Co (2nd sphere), respectively. The amorphous sample has similar first coordination as the crystalline $NiCo_2O_4$, but drastic differences in the second shell due to the long-range disorder for amorphous structure. The second shell contains contributions from a large number of overlapping single-, as well as multiple-, scattering contribution. Therefore, with increased scattering events, the intensity of these peaks drops with increasing coordination. We should also notice that the first coordination shell is extended by 0.15 Å, which indicates a more open structure, which favors ion diffusion.

Figure 5 shows the electrochemistry performance of C@ amorphous Ni–Co oxide which is tested under three-electrode configuration using 6 M KOH aqueous as electrolyte. Cyclic voltammetry (CV) measurement can reveal the reaction mechanism. At a scan rate of 1 mV s^{-1} (Fig. 5a), two pairs of redox peaks are clearly observed, which are ascribed to the redox reaction based on Ni^{2+}/Ni^{3+} and Co^{2+}/Co^{3+} transitions. These peaks indicate that Faradaic redox reactions occupy the main pseudo-capacitive reaction process. At higher scan rate of 2 mV s^{-1}, potential shifting phenomena occur and become much distinct at the scan rate of 5, 10 and 20 mV s^{-1} (Fig. 5b), which was caused by electrode polarization. Owing to the multi-redox action sites, large capacitance may be exhibited by the electrode. Figure 5c, 5d shows the galvanostatic charge–discharge curves in the potential range of 0.1–0.4 V. The voltage plateaus match well with the redox peaks observed from the CV curves. At various current densities of 1, 2, 5, 10, 15 and 20 A g^{-1}, the calculated specific capacitances could reach to 1775, 1485, 1200, 855, 600 and 415 F g^{-1}, respectively (Fig. 5e). Figure 5f shows the cycling stability which was tested at 5 A g^{-1}; after 2000 cycles, the capacity retains 86% of the first cycle, and the Coulombic efficiency is always maintained at 92%, indicating that the electrode has good long-term cycling-stability.

To further evaluate the electrochemistry performance of the C@ amorphous Ni–Co oxide, it was assembled into the coin cell of the asymmetry supercapacitor, in which activated carbon is the anode and 2 M KOH is the electrolyte. The cell is tested in a potential range of 0–1.5 V. Figure 6a shows the galvanostatic charge–discharge curves, and it delivers specific capacitances of 83.4, 71.8, 65.4, 5.2 and 45.3 F g^{-1} at 0.2, 0.5, 1, 2 and 5 A g^{-1}, respectively (Fig. 6b). In the corresponding CV curves of Fig. 6c, a pair of redox peak is observed, which implies the pseudo-capacitive characteristic. With the increased scan rate from 1 to 10 mv s^{-1}, the intensity of the peaks become larger, and is the fast charge/discharge characteristic of the asymmetric supercapacitor. As shown by the Ragone plot (Fig. 6d), the cell delivers high energy density and power density, for instance, at 1 A g^{-1} the energy density and power density are 73.5 Wh kg^{-1} and 806.7 W kg^{-1}, respectively, which are comparable

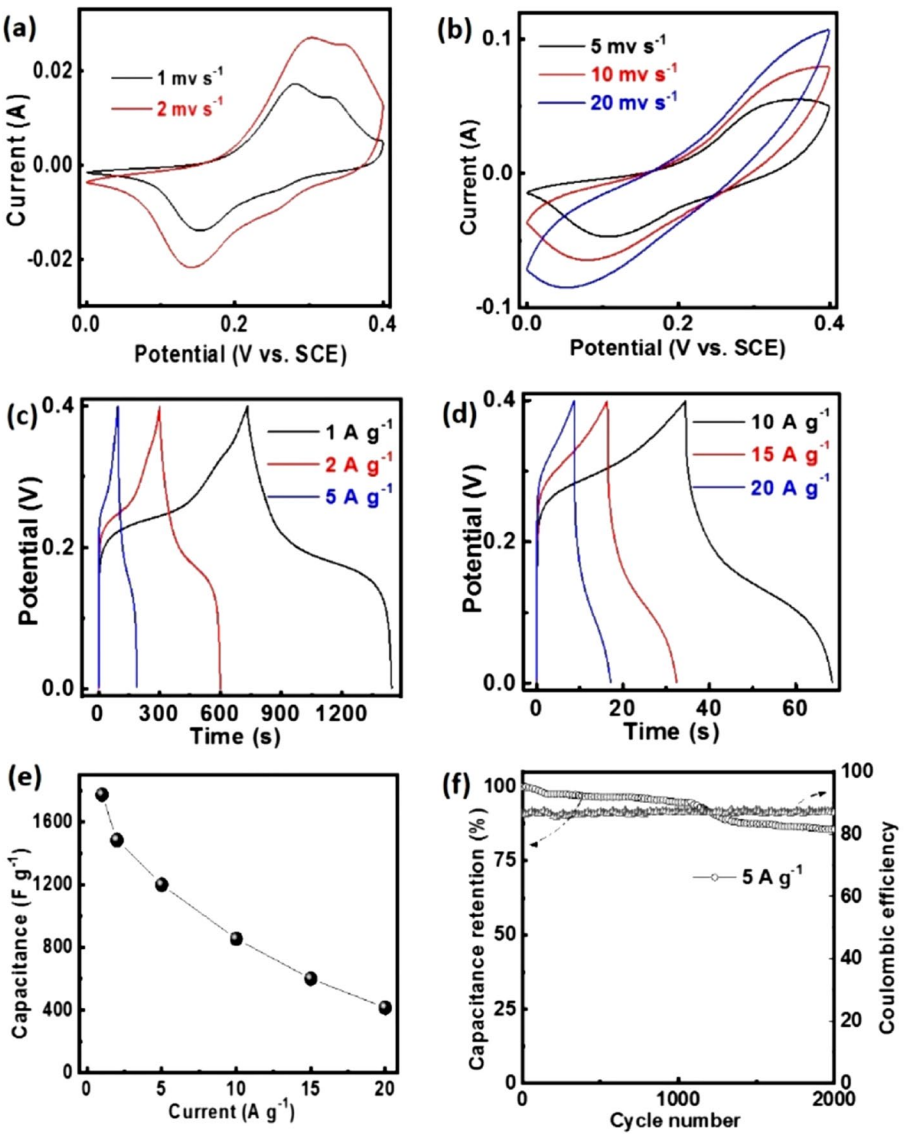

Fig. 5 **a**, **b** CV curves; **c**, **d** charge and discharge curves; **e** specific capacitance as a function of the current; and (f) cycling performance at the current density of 5 A g^{-1} of C@ amorphous Ni–Co oxide electrode tested at standard three-electrode configuration in aqueous electrolyte

with other values reported by $NiCo_2O_4$-based asymmetric supercapacitors. [12–17]

The supercapacitor performance of crystal $NiCoO_2$ electrode is shown in Fig. 6e, f, which is tested at three-electrode as that as C@ amorphous Ni–Co oxide electrode. $NiCoO_2$ electrode shows obvious redox peaks on the CV curves (Fig. 6e), which indicates the pseudo-capacitive features, but the current values are lower than that of the amorphous form (Fig. 5a, b). At 1, 2 and 5 A g^{-1}, the capacitances calculated from the discharge curves are only 1141, 870 and 780 F g^{-1}, respectively (Fig. 5e), which is much lower than that of the amorphous one.

Electron and ion transfer are the two key factors for high energy supercapacitor. The C@ amorphous Ni–Co oxide has superior electron transfer and receiving sites, due to the following reasons: 1, the high conductivity was improved by the carbon coating layer (Fig. 1c); 2, the amorphous has rich electron receiving sites (Fig. 5a), due to the Ni^{2+}/ Ni^{3+} and Co^{2+}/Co^{3+} transitions that are observed in the CV curves as two pairs of redox peaks; 3, there is an additional localized charge transfer from Co to Ni which is deduced from EXAFS analysis (Fig. 4), in which the lower the intensity, the less is the transition possibility, meaning a greater number of electrons were transferred from the Co site to the conduction band of Ni. Besides the factor of electron, the amorphous sample is also favored for ion transfer: 1, the sphere composed of nanosheet has high surface area (94.7 m^2 g^{-1}); 2, according to the EXAFS analysis, the amorphous from has more open framework structure than the crystal one, which could enhance the ion transfer. These make the C@ amorphous Ni–Co oxide have outstanding electrochemical performance.

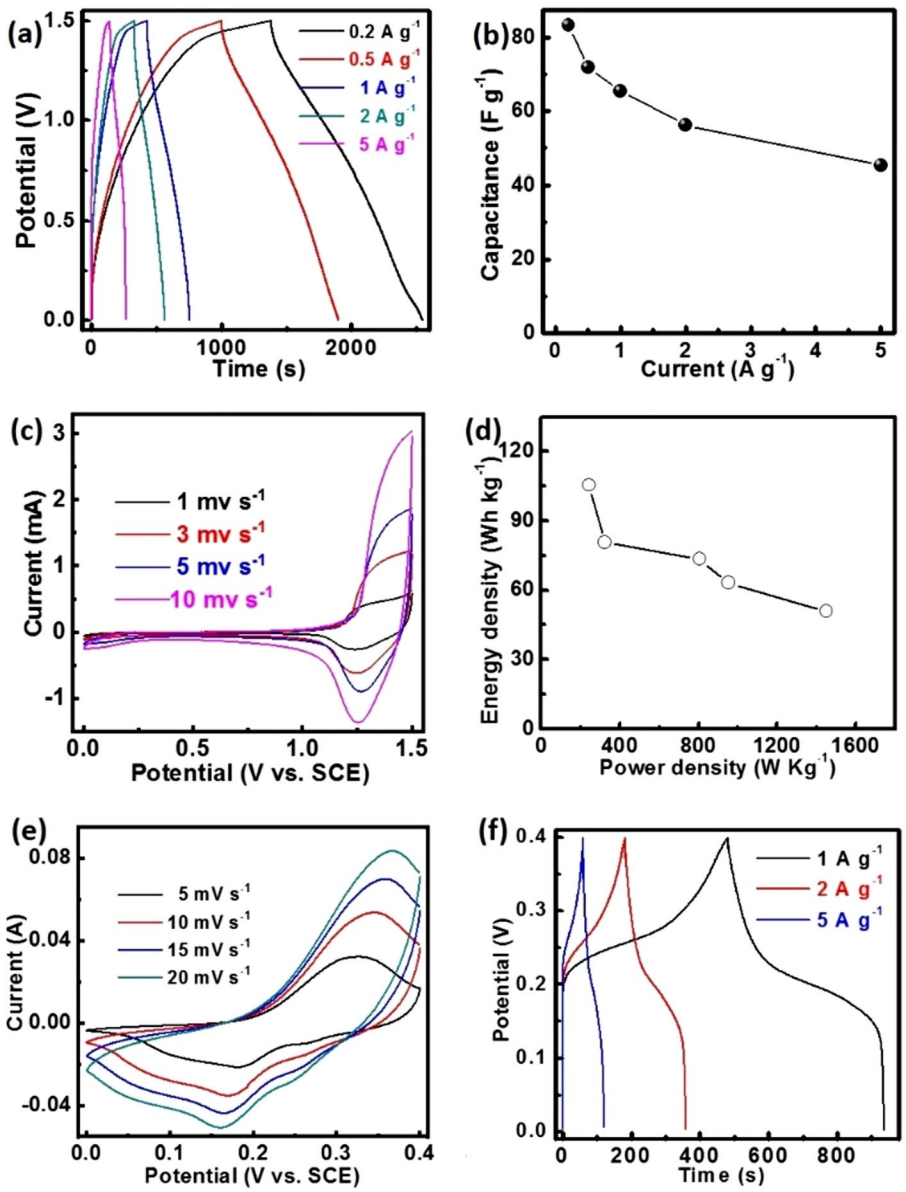

Fig. 6 **a** Charge and discharge curves; **b** specific capacitance as a function of the current; **c** CV curves; **d** Ragone plot of C@ amorphous Ni–Co oxide electrode tested at standard two-electrode configuration in aqueous electrolyte. **e** Charge and discharge curves and **f** CV curves of $NiCoO_2$ electrode tested at standard three-electrode configuration in aqueous electrolyte

4 Conclusions

In summary, carbon-wrapped amorphous Ni–Co oxide nanosheet is prepared by a hydrothermal method, followed by an annealing process in an Ar atmosphere. When the same hydrothermal precursor is annealed in air atmosphere, crystal $NiCoO_2$ is obtained. Due to the merits of high electrical conductivity and open framework structure, the amorphous form shows a high capacitance of 1775 F g^{-1} at 1 A g^{-1} in the three-electrode aqueous system, which is much higher than that of the crystal $NiCoO_2$ (1141 F g^{-1} at 1 A g^{-1}). The amorphous form also exhibits high energy density of 73.5 Wh kg^{-1} at the power density of 806.7 W kg^{-1} in the asymmetric supercapacitors. The advantage of a more open framework structure of the amorphous than that of the crystal form would make the amorphous form more suitable as an electrode of energy storage devices.

Acknowledgements The authors acknowledge the financial support from the Fund for Natural Science Foundation of Shaanxi Provincial Department of Education (No.20JS042).

References

1. G. Jialin, P. Zheng, Appl. Phys. A **127**, 509 (2021)
2. A. Lai, Y. Chu, J. Jiang, Y. Huang, S. Hu, Q. Pan, F. Zheng, J. Wang, J. Li, H. Wang, Q. Li, Electrochim. Acta **414**, 140161 (2022)
3. T. Guo, D. Zhou, L. Pang, S. Sun, T. Zhou, J. Su, Small **18**, 2106360 (2022)
4. K. Li, J. Li, Q. Zhu, B. Xu, Small Methods **6**, 2101537 (2022)

5. K. Dong, Z. Yang, D. Shi, M. Chen, W. Dong, J. Mater. Sci.: Mater. Electron **33**, 13547 (2022)
6. N. Du, Y. Xu, H. Zhang, J. Yu, C. Zhai, D. Yang, Inorg. Chem. **50**, 3320 (2011)
7. M. Isacfranklin, S. Daphine, R. Yuvakkumar, L. Kungumadevi, G. Ravi, A.G. Al-Sehemi, D. Velauthapillai, Ceram. Int. (2022). https://doi.org/10.1016/j.ceramint.2022.05.123
8. S. Peng, L. Li, H.B. Wu, S. Madhavi, X.W. Lou, Adv. Energy Mater. **5**, 1401172 (2015)
9. L.-Q. Mai, F. Yang, Y.-L. Zhao, X. Xu, L. Xu, Y.-Z. Luo, Nat Commun **2**, 381 (2011)
10. M. Li, W. Xu, W. Wang, Y. Liu, B. Cui, X. Guo, J. Power Sources **248**, 465 (2014)
11. A. Pendashteh, S.E. Moosavifard, M.S. Rahmanifar, Y. Wang, M.F. El-Kady, R.B. Kaner, M.F. Mousavi, Chem. Mater. **27**, 3919 (2015)
12. Z. Fan, B. Wang, Y. Xi, X. Xu, M. Li, J. Li, P. Coxon, S. Cheng, G. Gao, C. Xiao, G. Yang, K. Xi, S. Ding, R.V. Kumar, Carbon **99**, 633 (2016)
13. T. Peng, Z. Qian, J. Wang, L. Qu, P. Wang, Phys. Chem. Chem. Phys. **17**, 5606 (2015)
14. R. Zou, M.F. Yuen, Z. Zhang, J. Hu, W. Zhang, J. Mater. Chem. A **3**, 1717 (2015)
15. L. Shen, Q. Che, H. Li, X. Zhang, Adv. Funct. Mater. **24**, 2630 (2014)
16. Y. Zhu, Z. Wu, M. Jing, H. Hou, Y. Yang, Y. Zhang, X. Yang, W. Song, X. Jia, X. Ji, J. Mater. Chem. A **3**, 866 (2015)
17. L. Shen, L. Yu, X.-Y. Yu, X. Zhang, X.W. Lou, Angew. Chem. Int. Ed. **54**, 1868 (2015)
18. J. Zhu, Z. Xu, B. Lu, Nano Energy **7**, 114 (2014)
19. H. Guo, L. Liu, T. Li, W. Chen, J. Liu, Y. Guo, Y. Guo, Nanoscale **6**, 5491 (2014)
20. Y. Chen, J. Zhu, B. Qu, B. Lu, Z. Xu, Nano Energy **3**, 88 (2014)
21. X. Xu, B. Dong, S. Ding, C. Xiao, D. Yu, J. Mater. Chem. A **2**, 13069 (2014)
22. L. Peng, H. Zhang, L. Fang, Y. Bai, Y. Wang, A.C.S. Appl, Mater. Interfaces **8**, 4745 (2016)
23. H.B. Wu, H. Pang, X.W. Lou, Energy Environ. Sci. **6**, 3619 (2013)
24. L. Wang, Y. Zheng, X. Wang, S. Chen, F. Xu, L. Zuo, J. Wu, L. Sun, Z. Li, H. Hou, Y. Song, A.C.S. Appl, Mater. Interfaces s **6**, 7117 (2014)
25. A.-M. Alexander, J.S.J. Hargreaves, Chem. Soc. Rev. **39**, 4388 (2010)
26. P.D. Tran, T.V. Tran, M. Orio, S. Torelli, Q.D. Truong, K. Nayuki, Y. Sasaki, S.Y. Chiam, R. Yi, I. Honma, J. Barber, V. Artero, Nat Mater **15**, 640 (2016)
27. K.-C. Pham, Y.-H. Chang, D.S. McPhail, C. Mattevi, A.T.S. Wee, D.H.C. Chua, A.C.S. Appl, Mater. Interfaces **8**, 5961 (2016)
28. A. Mery, F. Ghamouss, C. Autret, D. Farhat, F. Tran-Van, J. Power Sources **305**, 37 (2016)
29. M. Fukuhara, T. Kuroda, F. Hasegawa, Sci. Rep. **6**, 35870 (2016)
30. L. Yu, N. Brun, K. Sakaushi, J. Eckert, M.M. Titirici, Carbon **61**, 245 (2013)
31. W. Wang, P. Gao, S. Zhang, J. Zhang, J. Alloys Compd. **692**, 908 (2017)
32. S. Okada, T. Yamamoto, Y. Okazaki, J.-I. Yamaki, M. Tokunaga, T. Nishida, J. Power Sources **146**, 570 (2005)
33. C. Gerbaldi, G. Meligrana, S. Bodoardo, A. Tuel, N. Penazzi, J. Power Sources **174**, 501 (2007)
34. E. Uchaker, Y.Z. Zheng, S. Li, S.L. Candelaria, S. Hu, G.Z. Cao, J. Mater. Chem. A **2**, 18208 (2014)
35. Q. Lu, Z.J. Mellinger, W. Wang, W. Li, Y. Chen, J.G. Chen, J.Q. Xiao, Chemsuschem **3**, 1367 (2010)
36. H. Li, Y. Gao, C. Wang, G. Yang, Adv. Energy Mater. **5**, 1401767 (2015)
37. C. Long, M. Zheng, Y. Xiao, B. Lei, H. Dong, H. Zhang, H. Hu, Y. Liu, A.C.S. Appl, Mater. Interfaces **7**, 24419 (2015)
38. C. Shang, S. Dong, S. Wang, D. Xiao, P. Han, X. Wang, L. Gu, G. Cui, ACS Nano **7**, 5430 (2013)
39. J.G. Kim, D.L. Pugmire, D. Battaglia, M.A. Langell, Appl. Surf. Sci. **165**, 70 (2000)